Chemical Engineering Journal 452 (2023) 139199

Contents lists available at ScienceDirect

Chemical Engineering Journal

journal homepage: www.elsevier.com/locate/cej

Cu_3PS_4: a sulfur-rich metal phosphosulfide with superior ionic diffusion channel for high-performance potassium ion batteries/hybrid capacitors

Sheng-Feng Ho, Hsing-Yu Tuan *

Department of Chemical Engineering, National Tsing Hua University, Hsinchu 30013, Taiwan

ARTICLE INFO

Keywords:
Metal sulfide
Potassium ion battery
Hybrid capacitor
Ionic channel
Diffusion

ABSTRACT

The emerging conversion-type chalcogenide anode materials for potassium ion storage may propose high theoretical specific capacity (>600 mA h g^{-1}) and high compatibility with electrolytes, but currently the reported performance falls behind this goal due to severe material pulverization, polysulfide shuttle effect, and slow potassium ion diffusion during a charge/discharge process. Here, we report that Cu_3PS_4, a sulfur-rich orthorhombic metal phosphosulfide, can achieve highly reversible multiple conversion reactions, including the formation of KP and K_2S along with 9 electrons transfer and efficient diffusion of potassium ions. Moreover, we introduce a layer graphite surface coating to enhance the overall conductivity of the electrodes, decrease the internal resistance, and render specific electronic channel with fast kinetic diffusion. During cycling, a tightly connected K-Cu—P—S junctions were formed to establish an ultra-stable heterostructure to entrap polysulfides in materials via an appropriate and uniform affinity. In electrochemical tests, Cu_3PS_4 potassium ion anodes exhibit the highest capacity of 649.3 mA h g^{-1} at a current density of 0.05 A/g, reaching 94.4 % of its theoretical capacity (687.3 mA h g^{-1}), and showed an ultra-stable 3000 cycle life and high-rate capability up to 8 A/g. Furthermore, the full battery and hybrid capacitor show attractive energy density and long cycle life of 82.5 W h kg^{-1} for 800 cycles and 80.3 W h kg^{-1} for 5000 cycles, respectively. This work provides promising results for metal phosphosulfide applications in high-efficiency potassium-ion storage devices, and may also be instructive for material advancements in related energy fields.

1. Introduction

Lithium-ion batteries with long cycle life [1–3] and high-power density [4–7] have breakthrough applications in electrified transportation and portable electronics [8]; however, the insufficient lithium content in the earth's crust and the high cost of lithium metal remain a challenge for widespread applications in the future [9–11]. In this scenario, potassium-ion batteries have become the alkali metal analogs of electronic conversion technology in recent years due to their similar physical and chemical properties to lithium-ion batteries [12]. Their low cost ascribed to the abundant resources (1.5 wt%), and the standard redox potential of K^+/K (–2.93 V) is higher than that of Li^+/Li (–3.04 V), enabling its application to work at high operating voltages and higher energy density in full cells [13–17]. In addition, the similar intercalation chemistry endows potassium-ion batteries with chemical reactions at high potential [18–20]. On the other hand, low-cost aluminum foil can be used as a current collector, so that the weak Lewis acidity of potassium ions enhances their diffusion in various electrolyte [21,22], and effectively relieves the polarization at the interface between the electrolyte and the electrode [23–26]. Nonetheless, the large atomic radius of potassium ions makes it difficult to intercalate into electrode materials, resulting in less specific capacity and accompanying poor kinetic response and rate performance [27,28].

Transition metal sulfides which possess high theoretical volume capacity, intrinsic conductivity and ionic conductivity have received great attention in recent years [29–36], such as SnS_x [37,38], CuS_x [39], MoS_x [40], TiS_x [41] and so on. Since the M−S bond between MS_x is weaker than the M−O bond, and the final conversion product M_2S_x produced by MS_x during the charge–discharge reaction is more conductive than M_2O, metal sulfides with better kinetic properties are more suitable for potassium ion battery systems than metal oxides [42,43]. However, direct use of these materials exhibits poor cycling performance due to ineffective activation. Carbonaceous materials are widely used to the form a layer structure on the electrode surface, thereby simultaneously improves the overall conductivity of the electrode [44–47]. Together with the increase of active sites in the electrolyte, the active material can

* Corresponding author.
E-mail address: hytuan@che.nthu.edu.tw (H.-Y. Tuan).

https://doi.org/10.1016/j.cej.2022.139199
Received 21 July 2022; Received in revised form 26 August 2022; Accepted 10 September 2022
Available online 15 September 2022

transport potassium ions more efficiently during cycling, which further improves the rate performance [48]. Nevertheless, transition metal sulfides often face the redox shuttle effect during the charge–discharge process, resulting in the formation of polysulfides that repeatedly dissolve in the electrolyte, leading to continuous loss of active materials during chemical reactions. Although carbon-coated materials can effectively suppress the collapse of the structure, the non-polar carbon framework is difficult to dissolve polysulfides through physical adsorption. It has been pointed out that physical adsorption and chemical bonding of polysulfides are the most commonly applied solutions, but doping other host materials may increase the overall active material weight and reduce the volumetric capacity of the electrode at the same time [49,50]. Among binary transition metal sulfides, few anode materials can effectively alleviate the polysulfide dissolution problem, resulting in mediocre performance in full-cell applications or potassium-ion hybrid capacitors (PIHCs). To this situation, several recent studies have proved that the polyatomic synergistic effect induced via the addition of metal elements can increase the contact area between the active material and the electrolyte [51,52], and shorten the diffusion distance of metal ions. Compared with monometallic sulfides, the addition of elements such as phosphorus, antimony, bismuth and some VA group element may boost the synergistic effect and can provide more redox active centers [53,54], and render fast electronic conduction.

Ternary transition metal sulfides are intrinsic variants of binary transition metal sulfides with high electrical conductivity and more redox active sites relative to metal oxides and metal hydroxides. Ternary sulfides with 3d orbitals may enable the existence of many Lewis acids and bases between polar materials and polysulfides, so that the migration of polysulfides is greatly restricted by chemical bonds. Compared with polar oxides, polar sulfides have higher electronic conductivity, so they may be more suitable as sulfur frameworks, which can also effectively adsorb polysulfides. For example, Kim *et al.*, applied the ternary transition metal sulfide $NiTi_2S_4$ to Li-ion batteries and found that insoluble Li_2S is formed during the intercalation/de-lithiation reaction instead of LiPSs [55]. Guo *et al.* found that the ternary transition metal sulfide (FCN111) has surface electro-positivity, and its strong Lewis acid-base interaction can further avoid the formation of LiPSs [56]. Yan *et al.* found that the ternary material $MnCo_2S_4$ synthesized by sulfurization can utilize its unique crystal structure to prevent the electrode powder agglomeration, thereby inhibiting the shuttle effect [57]. Based on the above viewpoints, the effective combination of ternary transition metal sulfide and carbon layer can simultaneously stabilize the electrode and overcome the redox shuttle effect, prolonging anode life span and rate performance of the electrode.

In this study, an orthorhombic ternary metal phosphosulfide Cu_3PS_4/G were prepared by high-energy ball milling with a specific molar ratio of copper, phosphorus, and sulfur as precursors, and graphite. By enhancing the synergistic effect of elements of the ternary materials to improve the diffusivity of potassium ions, and through simulation and experimental mutual corroboration, the advantages of Cu_3PS_4/G compared with CuS/G were confirmed and the challenges such as the shuttle effect and long-term cycling performance of metal sulfides were resolved. The theoretical calculation shows that potassium ions have a low-energy barrier in the material to effectively capture potassium polysulfides through the synergistic effect of ternary materials during conversion reaction. In addition, Cu_3PS_4/G can also reach the highest specific capacity 649.3 mA h g^{-1} at 50 mA g^{-1} as well as the high electrochemical performance in other aspects, including capacity retention (CR), initial Coulombic efficiency (ICE), long term cycle number, and high current density. Finally, we fabricated a full battery with Prussian blue ($K_xFe(Fe(CN_6))$) and a hybrid capacitor using activated carbon as a cathode, respectively. Both showed attractive energy density and long cycle life, which are 82.5 W h kg^{-1} at 800 cycles for batteries and 80.3 W h kg^{-1} at 5000 cycles for hybrid capacitor, respectively.

2. Results and discussion

2.1. Material characterization

The schematic illustration of the synthesis of pristine Cu_3PS_4 nanoparticles by high-energy ball milling was shown (Fig. 1a). We performed a two-step high-speed ball milling, firstly, Cu particles, P_2S_5, and sulfur powders were mixed in a zirconia jar with a stoichiometrically molar ratio of 6:1:3, the first ball milling is carried out in the state without oxygen, and the elements are forced to bond with extremely high energy. The second step ball milling not only coats the graphite evenly on the periphery of pristine Cu_3PS_4, but also grind the powder finely at high rotational speed so that it can be applied to the electrode material. The crystal structure of the as-synthesized pristine Cu_3PS_4 was analyzed by XRD (Fig. 1b), showing all the diffraction peaks of pristine Cu_3PS_4 consistent with the Rietveld refined results corresponding to the *Pmn*21 [31] space group, indexed to an orthorhombic crystal system. Given the fitting curves, no other peaks were observed except for the index, and the obtained lattice parameter of Cu_3PS_4 is identical to the theoretical value. Furthermore, the XRD pattern of Cu_3PS_4/G are shown (Fig. S1b). It is clear that Cu_3PS_4/G coated with layered graphite shows an obvious peak of graphite at the position where the 2 theta is 20.8°, indicating that the graphite and pristine Cu_3PS_4 form a uniform composite. The morphology of the as-prepared Cu_3PS_4/G is observed by scanning electron microscope (SEM) (Fig. 1c). It can be seen that the size of the nanoparticles of Cu_3PS_4/G ranges from 50 nm to 1 μm, and due to the high energy ball milling, the nanoparticle size of Cu_3PS_4/G with a non-fixed shape and larger aggregates can be observed in the SEM images. Local analysis of Cu_3PS_4/G by transmission electron microscopy (TEM) (Fig. 1d) revealed that the outermost layered graphite uniformly covers the material, maintaining the stability of the structure by forming a uniform complex. In addition, the selected area electron diffraction (SAED) (Fig. 1e) shows three ring patterns corresponding to (2 3 2), (2 1 3), (4 2 3) crystal planes, which is consistent with the diffraction peaks of the XRD result. The high-resolution TEM image of Cu_3PS_4/G was demonstrated (Fig. 1f), indicating the d-spacing of planes (2 1 0) and (0 0 2) with a corresponding lattice spacings of 0.315 nm and 0.304 nm, respectively. The white illustrated frame elucidates the boundary where the Cu_3PS_4/G nanoparticles are uniformly covered by the graphite layer. In addition, we used X-ray energy dispersive elemental analysis (EDS) to analyze the nanoparticles captured by TEM. It can be seen that the three elements of copper, phosphorus and sulfur are uniformly distributed in the field (Fig. 1g). Among them, the signal intensities of copper and sulfur are similar, obviously more than that of phosphorus, consistent with the molar ratio of the elements contained in the Cu_3PS_4/G compound. Another area of the morphology of Cu_3PS_4/G nanocomposite (Fig. 1h) shows Cu_3PS_4/G covered by layer graphite uniformly as well. The d-spacing index demonstrates crystal plane of (0 0 2) and (2 1 1) with d-spacing of 0.304 nm and 0.28 nm, respectively (Fig. 1i). The XPS spectra were also used to qualitatively analyze the valence states of elements in Cu_3PS_4. The C orbital of Cu_3PS_4/G, and the C—C bond and C—P bond can be corresponded with the graphite coating (Fig. S3), while the peaks at binding energies 952.5 eV and 932.5 eV are mainly attributed to Cu $2p_{1/2}$ and Cu $2p_{3/2}$, from Cu-P and Cu-S bonds, respectively (Fig. 1j). Furthermore, the binding energies at 134.3 eV and 135.3 eV correspond to the splitting of the P 2p core orbital, distinguished as P—C bond and P—S bond originating from the graphite and pristine Cu_3PS_4 (Fig. 1k). From the result, it is evident that graphite may form a chemical bonding with pristine Cu_3PS_4, attributed to the high-energy ball milling process. In the spectrum of S 2p (Fig. 1l), characteristic peaks at 168.6 and 161.9 eV can be considered as SO_x and S $2p_{3/2}$.

2.2. Electrochemical tests and analysis

We evaluate the electrochemical performance of Cu_3PS_4/G

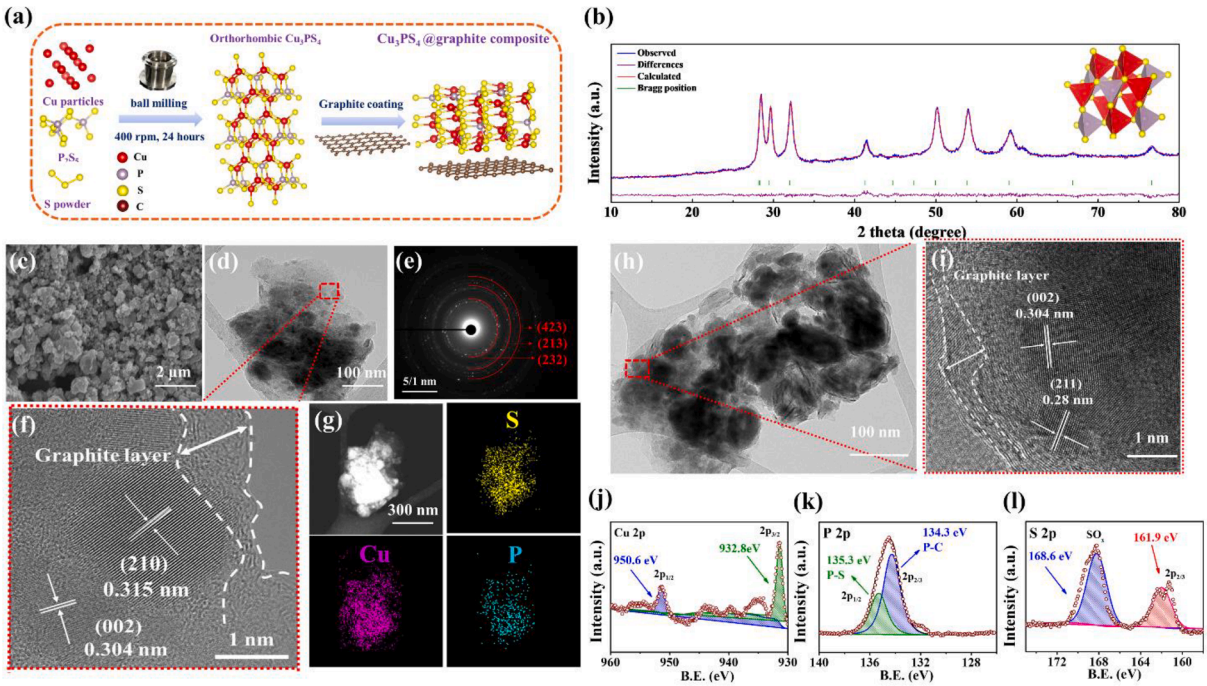

Fig. 1. Material characterization of Cu_3PS_4/G. (a) Schematic illustration of the high energy ball milling synthetic process. (b) Powder XRD for refinement spectra with crystal structure. (c) SEM images at high magnification. (d, h) TEM images. The inset specifies the proposed region coated with layer graphite. (e) SAED ring pattern. (f, i).

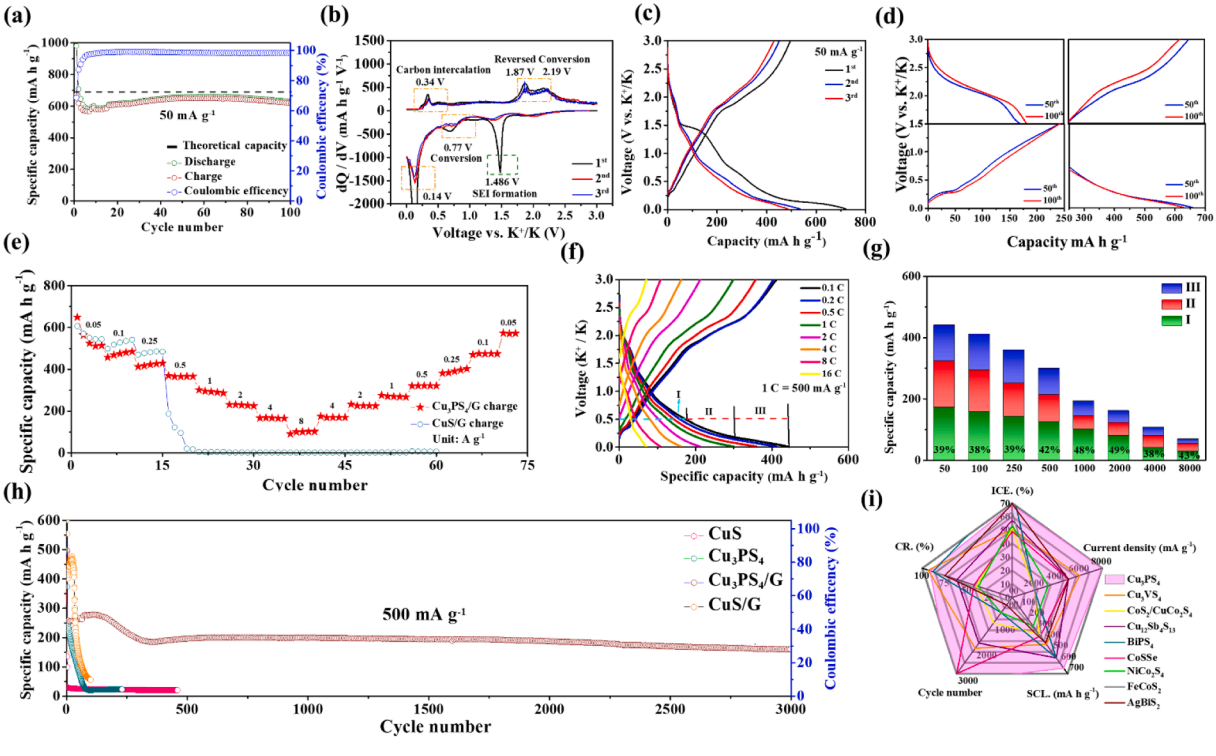

Fig. 2. Electrochemical performance test. (a) Cycling performance at 50 mA g^{-1}, and the theoretical capacity of Cu_3PS_4/G to compare the difference with the result. (b) dQ/dV curves at the first three cycles. (c) Galvanostatic charge–discharge curves of Cu_3PS_4/G at 1st, 50th, and 100th cycle. (d) The segmentation of the galvanostatic charge–discharge curves at 50th and 100th cycle. (e) Rate performance of Cu_3PS_4/G and CuS/G at eight current densities. (f) Rate performance serving as charging-discharging profile for Cu_3PS_4/G. (g) The bar chart of the calculated capacity contribution at various stage of the QV curves. (h) Long-term cycling performance of Cu_3PS_4/G at 500 mA g^{-1}. (i) Radar chart of the comparison of recent ternary metal sulfides applied in PIBs.

composite by assembling a coin-type half-cell tested at voltage ranging from 0.01 V ~ 3 V. In general, the reversible specific capacity directly reflects the utilization efficiency of the conversion products, *i.e.*, KP and K_2S, while the cycle life shows how the electrode suppresses the redox shuttle effect induced by the chalcogenide electrode. The galvanostatic charge–discharge curves of pure graphite is shown (Fig. S4), and the result confirms that graphite may render a reversible capacity of 107 mA h g^{-1}, which is 38 % of its theoretical capacity. Therefore, based on the proportion of graphite to the Cu_3PS_4, graphite provides a capacity of approximately 30 mA h g^{-1} to the Cu_3PS_4/G electrode. Therefore, layer graphite may not significantly influence the reversible capacity of Cu_3PS_4, but decrease the overall resistance of the electrodes during chemical reaction. Furthermore, it provides effective activation and protection to Cu_3PS_4, allowing a stabler charge–discharge process. In addition, the CV curves of Cu_3PS_4/G at the scan rate of 0.1 mV s^{-1} is exhibited (Fig. S5). The result suggests that Cu_3PS_4/G electrode undergo reversible chemical reaction due to the overlap of curves. Except for the obvious difference at 1st cycle because of SEI formation, the result proves the excellent reversibility of the material. The cyclic performance of Cu_3PS_4 /G at low current density (50 mA g^{-1}) is demonstrated (Fig. 2a). It shows that the electrode obtains 69 % of the initial Coulombic efficiency, and delivers the highest capacity of 649.3 mA h g^{-1} at the 60th cycle, and maintains 617.8 mA h g^{-1} at 100 cycles. Notably, the reversible capacity reaches 94.4 % of the theoretical capacity (687.3 mA h g^{-1}) at 60 cycles, and is still as high as 90.0 % at 100 cycles. In order to analyze how the internal chemical reaction contributes to such a high reversible capacity, we plot a dQ/dV diagram of the galvanostatic charge–discharge curves in the first three cycle (Fig. 2b). First, there is a large peak difference around 1.48 V in the first cycle, which can be attributed to the growth of the solid electrolyte interface (SEI) resulted from irreversible reaction. Furthermore, the three curves are overlapped visibly at 0.77 V, we deduced that the first conversion reaction occurred at this potential, which may be the conversion of Cu_3PS_4/G into K_2S_4 and K_2S_3, while the peak at 0.14 V can be attributed to the formation of KP[58]. During the charging process, the plateau positions where the electricity is mainly contributed are 0.34 V, 1.87 V, and 2.19 V. Among them, 0.34 V and 1.87 V are known from the references as the intercalation of carbon and conversion reaction of phosphorus[59], and 2.19 V is the conversion reaction of sulfur, both of which are reversible reactions. Furthermore, as can be seen from the height of the curve, the electrical contribution of phosphorus is greater than that of sulfur because it has a more pronounced redox reaction. Apart from the difference in the first cycle due to unfavored side reactions, the good reversibility of the electrode is from the degree of superposition owing to the overlap of the curves. In order to show that the plateau is still obvious after many cycles, we plot the charge–discharge curves in 50th and 100th cycle and compare them with the 1st cycle (Fig. 2c). Except for the irreversible side reactions in the first cycle and the formation of the SEI film, the locations of the platforms are similar. If the specific potential interval is enlarged and viewed (Fig. 2d), the charge–discharge curves of the 50th and 100th cycles can be divided into two main platforms, corresponding to the multiple conversion reactions of S and P, respectively. The degree of superposition shows that the electrode has almost no overpotential, indicating that the charge transfer resistance (R_{ct}) is small during the phase transition. We also tested the rate capability of the electrodes at current densities ranged from 0.05 to 8 A g^{-1} (Fig. 2e). The reversible capacity of Cu_3PS_4/G are 563, 468, 416, 365, 301, 231, 167, and 90 mA h g^{-1}, at 50, 100, 250, 500, 1000, 2000, 4000, 8000 mA g^{-1}, respectively. After the current density is restored to 50 mA g^{-1}, the capacity can still be maintained 570.2 mA h g^{-1}, showing good retention after high rate. Furthermore, the pristine Cu_3PS_4 and CuS both perform poor by applying rate capability test (Fig. S6). The charge capacity of Cu_3PS_4 decay at 0.05 mA g^{-1}, which shows that it cannot be fully charged and discharged even at a low current density. On the other hand, although CuS can react stably, its capacity is only 81.5, 46.6, 31.1, 18.4, 8.9, 4.7, 4.1, 2.4 mA h g^{-1} at 0.05, 0.1, 0.25, 0.5, 1, 2, 4, 8 A g^{-1}, respectively, and the low capacity shows that pure CuS and CuS/G cannot withstand high current densities. The charge–discharge curve of rate performance shows obvious plateau at high current density with low overpotential (Fig. 2f), indicating good reaction kinetics and stable diffusion ability of potassium ions. We divide the charge–discharge curve of rate performance into three main stages to analyze the degree of capacitance contributed by the conversion reaction respectively (Fig. 2g). The conversion reaction of phosphorus corresponded to stage I, and the conversion reaction of sulfur (K_xS_y) at stage II contributed the capacitance value. As for stage III, it consists of carbon intercalation and conversion reaction. The result shows that stage I provide the most percentage of capacity of about 40 %, while stage II contributes for about 30 % of the capacity. The bar further confirms that the reversible capacity is mostly contributed through the conversion reaction. As a result, we believe that more redox active sites are ionic and electronically continuous diffusion paths, contributing to the enhanced storage capacity of potassium ions and their migration in the electrode. Finally, we tested the long-term test at 0.5 A g^{-1} (Fig. 2h), showing that Cu_3PS_4 /G can still deliver a reversible capacity of about 180 mA h g^{-1} with an average Coulombic efficiency of 99.97 % for over 3000 cycles. The high Coulombic efficiency is attributed to the surface treatment of the structure and the uniform contact with electrolyte [60]. On the contrary, the binary CuS and the CuS/G exhibited poor cycling performance as their reversible capacity dropped to below 60 mA h g^{-1} after 100 cycles, with 98.55831 % of the average Coulombic efficiency at 100 cycle. In addition, CuS and the CuS/G present poor behaviors by applying different electrolyte (Fig. S7), indicating the inferior compatibility of the electrolyte and the material. The above results conclude that Cu_3PS_4/G has outstanding performance in both long-term cycle test and low-rate capability. As a result, we illustrate the radar chart of recent research of ternary metal sulfides in potassium-ion battery [61–68]. The electrochemical performance comparison of Cu_3PS_4/G and other ternary metal sulfides is demonstrated (Fig. 2i), including low-rate specific capacity (SCL), capacity retention (CR), initial Coulombic efficiency (ICE), long term cycle number, and high current density applied during rate performance test. As shown from the radar chart, this work obtained the largest area after comparing the five precise indicators. Aside from a leading performance of low-rate specific capacity, Cu_3PS_4/G anode exhibits a high initial Coulombic efficiency and shows its stability of rate capability at the highest current density. This result shows the appreciable electrochemical performance in many aspects among ternary metal sulfides through overcoming the redox shuttle effect and poor kinetic behavior.

2.3. Reaction mechanism of Cu_3PS_4/G

We analyze the crystal structure of the charge/discharge product at various voltages (Fig. 3a). When the electrode was discharged from the open-circuit voltage to 1.5 V, the first-step conversion reaction of Cu_3PS_4/G was initiated. We found that the diffraction peaks of the original material disappeared, and the peaks of KP (PDF #04–003-7018), K_2S_4 (PDF #00–030-0992) and K_2S_3 (PDF #04–007-0574) were located at the positions of 30.8°, 37.6°, and 54.4°, respectively, and their corresponded crystal planes were (1 1 2) and (3 3 2). As the potassium ions constantly inserted into the electrode, the voltage dropped to 0.01 V, *i.e.*, the fully-inserted state. It can be observed that the diffraction peak of KP is larger, and the phase of the first conversion reaction also disappears, confirming that KP is the final reduction product. Then, when the electrode was charged to 2 V, the first-step reversal reaction occurred. First, the diffraction peak of KP at 30.8° became significantly wider and smaller, and the peak of K_2S_3 appeared, indicating that the KP reversal conversion product formed. Finally, when the voltage reaches 3 V, only the switching phase of K_2S_3 and K_2S_4 can be observed, so we infer that this is a reversible switching reaction. For some phases with poor crystallinity, we applied XPS and Raman for qualitative analysis. The ex-situ Raman spectra at discharge state and charge state is

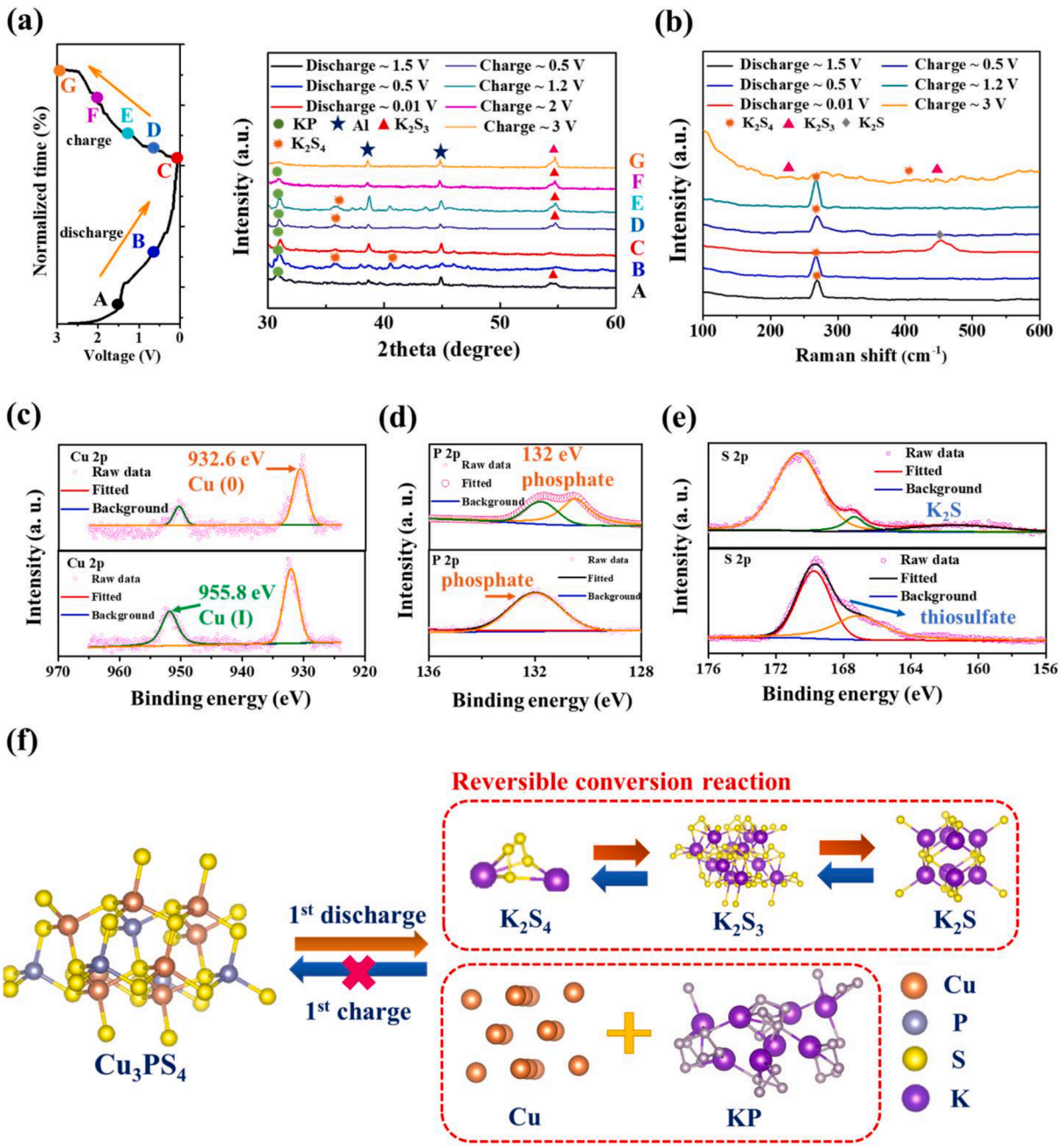

Fig. 3. Ex-situ analysis of the reaction mechanism of Cu_3PS_4. (a) Ex-situ XRD pattern at various stages of discharge(A-C)-charge(D-G) and the corresponding *T*-V curves. (b) Ex-situ Raman spectra at various stages of charge–discharge reactions. (c-e) Ex-situ XPS spectra at fully-discharged (0.01 V) and charged (3 V) state of Cu 2p, P 2p, S 2p orbital. (f) Schematic illustration of the multiple reaction mechanism of Cu_3PS_4/G. The crystal structure displays the reaction product at different stage.

exhibited respectively (Fig. 3b). A peak of K_2S_x appears at 270 cm^{-1} of Raman shift, and the 450 cm^{-1} peak when discharging to 0.01 V can be referred to K_2S. While the electrode charge back to 1.5 V, the reversible conversion reaction occurs, showing similar peak compared with the discharge curve. As a result, K_2S is being deduced also as a final product of the conversion reaction. To further elucidate the perspective, we used ex-situ XPS to see the valence state of electrode (Fig. 3c–e). The binding energies of 932.5 eV and 952.5 eV correspond to 0-valent copper and 1-valent copper (Fig. 3c), confirming the exsolution of copper [69]. In addition, it shows that the state of complete de-potassiation of mono-valent copper and zero-valent copper still exists at the electrode, which confirms the inference of reversible conversion reaction. The phosphate formed at the binding energy of 132 eV may be KP phase (Fig. 3d). Moreover, thiosulfate generated at the binding energy of 167.5 eV and 171.5 eV for charging and discharging, respectively; and the peak at the binding energy of 161.5 eV is indexed to the phase state of K_2S (Fig. 3e). Finally, we demonstrate the crystal structure of the corresponding phase during charge–discharge process (Fig. 3f). It is evident of a reversible conversion reaction occurred after the 1st discharge.

To further elucidate the phase evaluation during reaction mechanism, we examine the fully charged (3 V) and discharged products (0.01 V). First, the visual topography uniformly wrapped by layered graphite at a fully discharged state is shown (Fig. 4a), indicating that the structure remains intact after complete chemical reaction. The SAED pattern can be assigned to (1 0 3) and (0 1 3) facets of KP, and (1 1 1) facet of Cu phase, consistent with the *ex-situ* XRD and *ex-situ* XPS results (Fig. 4b). The HRTEM image (Fig. 4c) clearly demonstrate the products of the conversion reaction after potassium ion insertion, agreeing with the

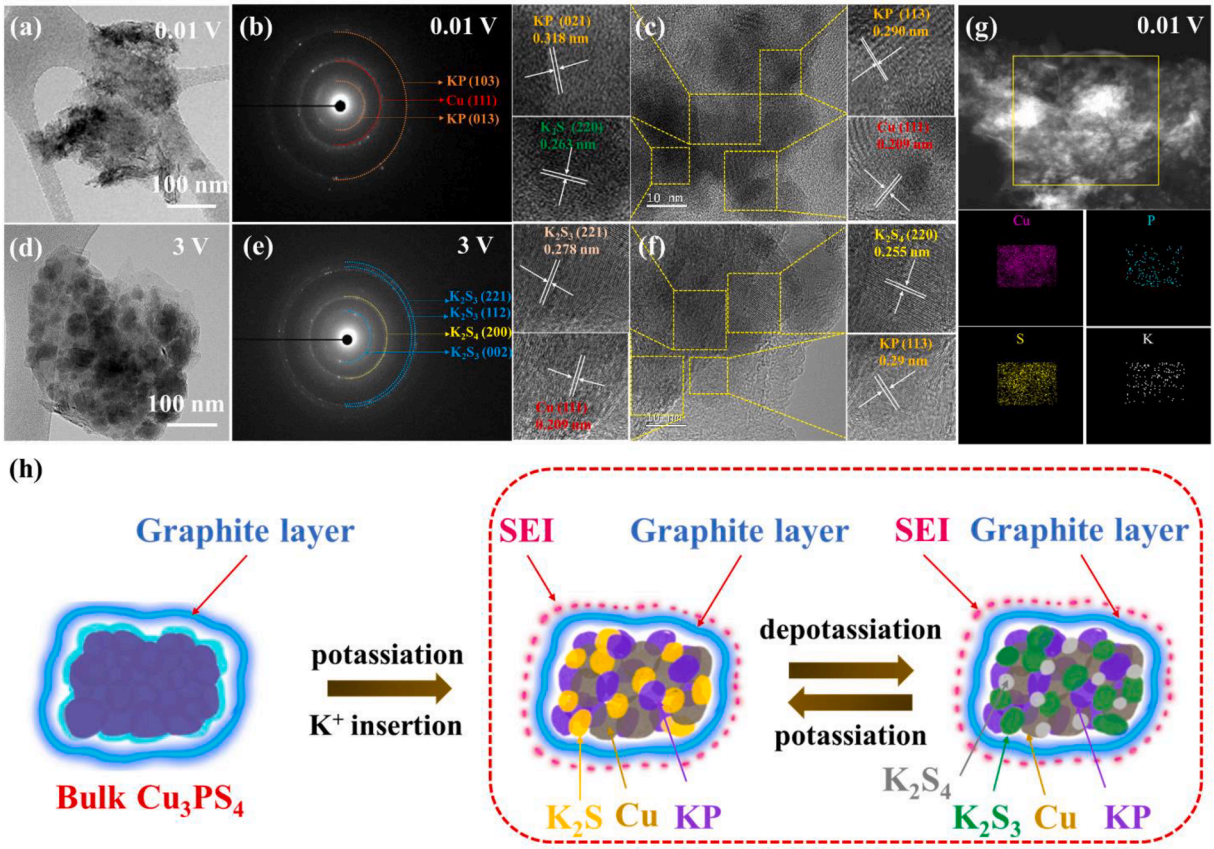

Fig. 4. Ex-situ TEM at fully potassiated (0.01 V) and de-potassiated (3 V) state of Cu_3PS_4/G. (a-c) TEM image, SAED pattern, and HRTEM image of Cu_3PS_4/G at 0.01 V. The yellow region insets in HRTEM display multiple junctions of the discharge product. (d-f) TEM image, SAED pattern, and HRTEM image of Cu_3PS_4/G at 3 V. The yellow region insets display multiple junctions of the charge product. (g) EDS mapping obtained at 0.01 V, showing the distribution of copper, phosphorus, sulfur, and potassium elements. (h) Schematic illustration of the morphological structure view during potassium ion insertion/extraction.

results of ex-situ XRD and XPS. At d-spacings of 0.263 nm and 0.318 nm, the lattice fringes of the conversion product can be assigned to the (220) plane of K_2S and the (021) plane of KP. In addition, the d-spacing of 2.09 Å can correspond to the (111) plane of Cu, confirming the existence of the reduction reaction of 0-valent copper. Furthermore, the fringe can be separated into adhesive junction, implying a tight contact among various phases. On the other hand, during the charging process, the low-magnification TEM image (Fig. 4d) shows that the electrode material formed a composite uniformly coated layered structure with a bulk-like morphology aggregated in the center. The SAED pattern (Fig. 4e) shows three distinct diffraction rings, corresponding to Cu (111), K_2S (200), K_2S_3 (200), respectively. The lattice fringe spacing of the reversibly transformed phase is shown (Fig. 4f), and their interplanar spacing is 0.278, 0.255, 0.209, and 0.29 nm, which corresponds to the crystal plane of K_2S_3 (221), K_2S_4 (220), Cu (111), and KP (113), respectively. In addition, the corresponding databases of K_2S, K_2S_3, KP and Cu have been attached in the supplementary information. It is worth mentioning that for Cu_3PS_4/G, in the reversible conversion reaction, the precipitation of copper is important and reasonable: in addition to allowing the electrode material to form a uniform composite, it can also improve the conductivity of the overall electrode. Finally, the HAADF image and EDS mapping results of Cu_3PS_4/G discharged to 0.01 V are shown (Fig. 4g), indicating the presence of copper, phosphorus, sulfur, and potassium without phase separation. By integrating the results of XRD, XPS, Raman spectra and TEM, we propose the following integrated equation:

Reduction.

Stage I: $Cu_3PS_4 + 3\,K^+ + 3\,e^- \rightarrow KP + 3\,Cu + K_2S_4$ + SEI formation (~1.5 V)

$K_2S_4 + 2\,K^+ + 2e^- \rightarrow 4\,K_2S_3$

Stage II: $K_2S_3 + 4\,K^+ + 4\,e^- \rightarrow 3\,K_2S$ (~0.01 V)

Oxidation

Stage III: $3\,K_2S \rightarrow K_2S_3 + 4\,K^+ + 4\,e^-$ (~2 V)

Stage IV: $4\,K_2S_3 \rightarrow 3\,K_2S_4 + 2\,K^+ + 2\,e^-$ (~3 V)

Finally, we exhibit the overall reaction path accompanied with the corresponding structure (Fig. 4h). During the potassiation process, a junction formed tightly and different discharge phases adhere with the other phases. Moreover, the reversible conversion reaction allows the existence of junction and the stable graphite layer prevent the collapse of structure.

2.4. Kinetic analysis of Cu_3PS_4/G

The excellent K^+ storage capacity and long-term cycling performance of Cu_3PS_4/G may be related to the pseudo-capacitance and diffusion behaviors at different rates. We measured and calculated its pseudocapacitive contribution by cyclic voltammetry (CV) at different scan rates, varied from 0.1 mV s^{-1} to 0.9 mV s^{-1} (Fig. 5a). The curves have similar shapes and trends, indicating that the electrochemical process in the electrode is rapid and reversible, with no obvious phase transition. To determine whether the current is dominated by surface reaction or diffusion reaction can be judged by the following formula:

$$i_p = av^b (b = 0.5 \sim 1.0) \quad (1)$$

where a and b are power-law variables, i_p corresponds to the peak current, and v is the scan rate. In addition, the b value is relatively more

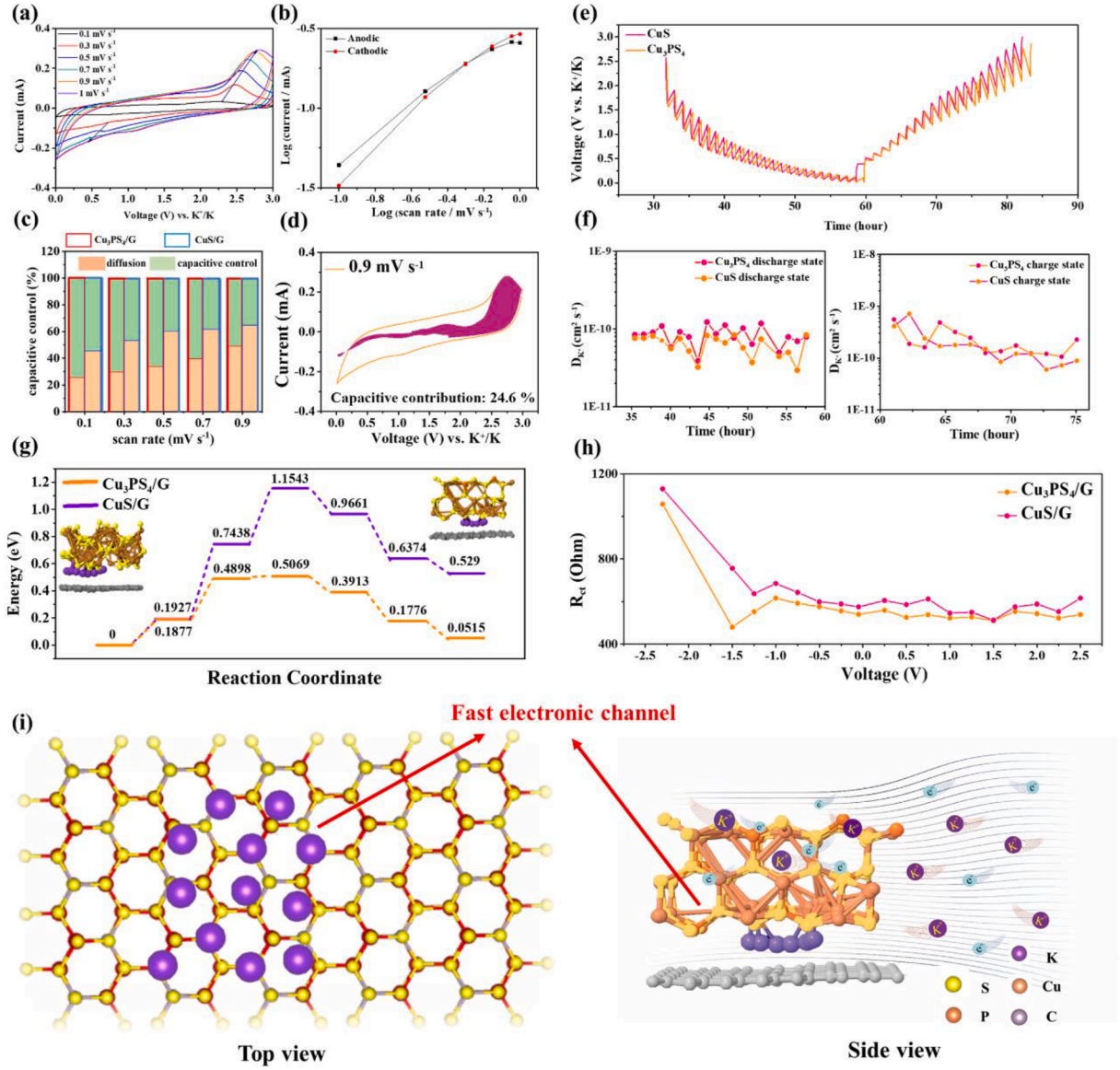

Fig. 5. Kinetic performance and potassium ion diffusion experiment of Cu_3PS_4/G. (a) CV curves at various scan rates. (b) Linear fitting profiles of log (i, peak current) vs log (v, scan rate). (c) Capacitance contribution of CuS/G and Cu_3PS_4/G. (d) The integral area of Cu_3PS_4/G displaying the potassium ion diffusion-controlled contribution at 0.9 mV s^{-1}. (e) GITT curves of CuS/G and Cu_3PS_4/G at 50 mA g^{-1}. (f) The diffusion coefficient calculated from the obtained GITT results. (h) DFT calculation of potassium ion diffusion energy barrier of CuS/G and Cu_3PS_4/G. (i) The top view and side view of electron–ion diffusion through ionic channel in orthorhombic Cu_3PS_4/G crystal structure.

important in this formulasince after taking the logarithm, the slope b value shows the kinetic contribution of the electrode surface. By taking the main peaks of the cathode and anode, their corresponding slope b values can be calculated to be 0.88 and 0.81, respectively (Fig. 5b). Therefore, we further use CV plots of different scan rates to quantify the contribution of the capacitive effect to the electrode as the diffusion control of potassium ion insertion or the contribution of the double layer capacitance. We use the relational equation for the calculation:

$$i = k_1 v + k_2 v^{0.5} \quad (2)$$

$$i/v^{0.5} = k_1 v^{0.5} + k_2 \quad (3)$$

Among them, k_1v of formula (2) represents the non-faraday reaction, while $k_1v^{0.5}$ represents the faraday reaction. By calculating the slope of k_1 and the intercept of k_2 and doing linear fitting, the main peak is the capacitive contribution of the reaction current at constant potential and the diffusion contribution. The capacitance contributions at different scan rates are shown (Fig. 5c), and the results show that the capacitance contributions from 0.1 mV s^{-1} to 0.9 mV s^{-1} are 25.6, 29.7, 33.9, 39.5, and 49.9 %, respectively. On the other hand, the CuS/G electrode is dominated by capacitive control; its capacitance contribution ratio corresponded to the CV curves at different scan rate (Fig. S8) is 45.5, 53.3, 60.2, 61.7, 64.9 %, respectively. Additionally, Cu_3PS_4/G also shows an 81.9 % capacitive control ratio at 0.5 mV s^{-1} (Fig. S9), explaining that layer graphite act as a superior electronic channel for potassium ion diffusion. In spite of a high contribution ratio, the Cu_3PS_4/G electrode fails to reach good reversibility at high current density due to poor diffusivity. The closed region of the CV curve fit at 0.9 mV s^{-1} is shown (Fig. 5d), the percentage of the enclosed area relative to the total area is 49.9 %, suggesting capacitance-controlled current is smaller than the surface-diffusion-controlled current, so that the kinetic reaction of the electrode is dominated by the diffusion-controlled current. According to the recent reports, electrodes are more likely to lose capacitance due to diffusion, and electrodes tend to contribute more to capacitance

at high current densities. However, high diffusion coefficient may allow potassium-ions to diffuse efficiently in the system, as a result, we utilize galvanostatic static intermittent titration (GITT) to further provide diffusion coefficients. The diffusion coefficient of GITT can be obtained from its curve and calculated by the following formula:

$$D_K^+ = 4/(\pi\tau)L^2((\Delta E^s)/(\Delta E_t))^2 \quad (4)$$

where τ, ΔEs, ΔEt, and L are denoted as the current pulse time (s), the constant voltage change induced by the current pulse, the potential change in the steady-state current pulse, and the electrode thickness, respectively. The GITT curve of Cu_3PS_4/G and CuS/G at a relaxation time of 20 min is shown (Fig. 5e), while the calculated diffusion coefficient value is shown (Fig. 5f). The diffusion coefficient is between 10^{-9} and 10^{-11}, and is closer to 10^{-10} ($cm^2\ s^{-1}$), which is higher than the value of CuS. In addition, the decrease in diffusion coefficient during potassium intercalation can be attributed to the influx of bulk potassium ions, resulting in structural expansion. Even so, Cu_3PS_4/G exhibits excellent diffusion behavior, corresponding to previous capacitive contribution tests, explaining how the electrode retains reversible capacitance under diffusion control and exhibits outstanding rate capability. In order to gain insight into how the reaction kinetics of potassium-ions in the electrode-material interface affects ion diffusion, we carried out density functional theory (DFT) calculations to study the K^+ storage capacity and the internal energy barrier coefficient. First, the construction models of Cu_3PS_4/G and CuS/G are shown (Fig. 5g). It is worth mentioning that these models all calculate similar total energies, indicating relative stability in the natural state. In addition, we select the (220) crystal plane observed by HRTEM, constructed a potassium ion transport channel, and simulated its possible diffusion pathway, and calculated the associated migration energy. We can find that the Cu_3PS_4/G has a lower site energy of 1.2 eV than that of CuS/G, which is approximately 0.5 eV in diffusion pathway, proving that the Cu_3PS_4/G possesses a faster ion diffusion due to low energy barrier especially at the surface, which is also coherent to the results measured by GITT. The above result may also be corresponded with the diffusivity of binary CuS/G and ternary Cu_3PS_4/G, demonstrating the advantage of Cu_3PS_4/G during chemical reaction, so that Cu_3PS_4/G is able to perform a better electrochemical performance than CuS/G. Finally, the resistance of the electrode is reduced and the capacitance value of the diffusion loss can be compensated. To confirm this inference, we used ex-situ electrochemical impedance spectroscopy (EIS) to measure the resistance change of Cu_3PS_4/G before electrochemical reaction. Before cycling, the R_{ct} of Cu_3PS_4/G is significantly large, about 4000 Ohm (Fig. S10). Furthermore, we used the in situ electrochemical impedance spectroscopy to test the continuous variation of R_{ct} value of Cu_3PS_4/G (Fig. 5h). The above results shows that the barriers to charge transfer and diffusion of Cu_3PS_4/G are extensively reduced during potassiation/de-potassiation. When discharging from OCV to 1.75 V, the R_{ct} value of the electrode is large and continues to rise when discharging to 1.25 V due to the formation of the SEI layer and the irreversible conversion reaction; however, when the electrode is fully discharged (0.01 V), its R_{ct} is reduced to about 500 O again. To image the above-mentioned results and understand the fast diffusion during charge–discharge process, we illustrate the Cu_3PS_4/G crystal structure in various angle. The top view and the side view of the potassium ion diffusion pathway are proposed (Fig. 5i). The large potassium ions are able to mobile through the crystal, and the layer graphite provides an electronic channel for electrons and ions since more active sites enhance redox reaction process. Therefore, the electrodes can sustain at a high current density, behave a superior potassium ion storage, and reduce the hinderance of the structure during chemical reaction.

2.5. Potassium polysulfides adsorption experiment

We conducted a chemical adsorption method to show the intense entrapment effect of pristine Cu_3PS_4, CuS (Fig. S11), Cu_3PS_4/G, and CuS/G composite toward potassium polysulfides. The experiments were executed by adding 30 mg K_2S to 5 ml DMC solution, and after a well dispersion, 40 mg of the testing material was added separately to start a 4-hour suspension (Fig. 6a). It is obvious that after 4 hours, the color of K_2S contained electrolyte with Cu_3PS_4/G and pristine Cu_3PS_4 transformed from light yellow to pure solution, whereas CuS/G has inconspicuous color difference compared with the original state. Thus, the result implies that Cu_3PS_4/G performs a stronger interaction with potassium poly-sulfates, while CuS/G composite exhibited ineffective entrapment effect. Moreover, we constructed various polysulfides (K_2S_y) and simulated the adsorption energies of the two materials for these polysulfides. The simulation result in a bar chart is demonstrated (Fig. 6b), and the adsorption energies of Cu_3PS_4/G to polysulfides are smaller than the value of CuS/G (Fig. 6c). Although the adsorption energy of Cu_3PS_4/G is not as high as that of CuS/G, in a typical chemical reaction, K_2S_x experience the de-sulfurization steps, which are all elementary reactions, while the active material serves as active sites to accelerate the decomposition of K_2S_x. As a result, the adsorption energy should maintain in a certain range of value without over-fluctuating to enable the electrode to react effectively. In this case, the utilization of sulfur can be enhanced during phase transformation, and thus improve the electrochemical performance.

2.6. In-depth discussion between the electrochemical result and analysis

Therefore, Cu_3PS_4/G has an unique kinetic behavior and the special material science during chemical reaction. During the charge and discharge process of the battery, ions and electrons will participate in chemical reactions in multiple diffusion paths that are beneficial to each other. From the results provided by DFT, we conclude that the material has good rate capability due to its excellent potassium ion diffusivity, which can effectively transfer charges even at very high current densities. In addition, we can infer that Cu_3PS_4/G not only can absorb polysulfides but also prevent them from dissolving in the liquid electrolyte. The Cu_3PS_4/G has a relatively stable chemical reaction to enable the material to capture the polysulfides generated during charge/discharge process and expand the utilization efficiency of K_2S_x, guaranteeing an ultra-stable electrode during cycling process. During the charge and discharge process, ions and electrons will participate in chemical reactions in multiple diffusion paths that are beneficial to each other. Through the effective diffusion paths simulated by DFT calculations, it is known that the formation of Cu_3PS_4/G along the diffusion pathway of the z-axis of the intersecting structure has the lowest diffusion energy barrier. Moreover, it has been suggested that more synergistic elements in the ternary material can provide a better ion exchange mechanism in the process of potassiation/de-potassiation of potassium ions, and increase different active sites, thereby enhancing the chemical reaction rate. Based on the above theoretical and experimental results, it can be concluded that potassium ions have outstanding diffusion ability in Cu_3PS_4/G anode compared with CuS, and the ratio of diffusion to capacitance contribution at high scan rate is close to 1:1, still possessing excellent rate performance. Despite that several studies related to the material based on diffusion control have demonstrated instability and capacitance loss at high current densities since the electrode may act as a capacitor and dominated by capacitive. However, due to the operation of the synergistic ion exchange mechanism and the open channels provided by orthorhombic Cu_3PS_4, it is possible to exhibit a fast Faradaic charge transfer process and excellent ion diffusion performance. Even at high current densities, the Cu_3PS_4 electrodes still maintain stable reversible reactions, which is rare in cases of diffusion-controlled based pseudocapacitive contributions. In addition, the diffusion coefficient of Cu_3PS_4 is one order of magnitude larger than that of CuS, which is 10^{-9} $cm^2\ s^{-1}$, and the diffusion energy barrier in each direction is much lower than that of CuS. These results enable the electrode to provide excellent charge storage performance and ion–electron transfer. By creating an

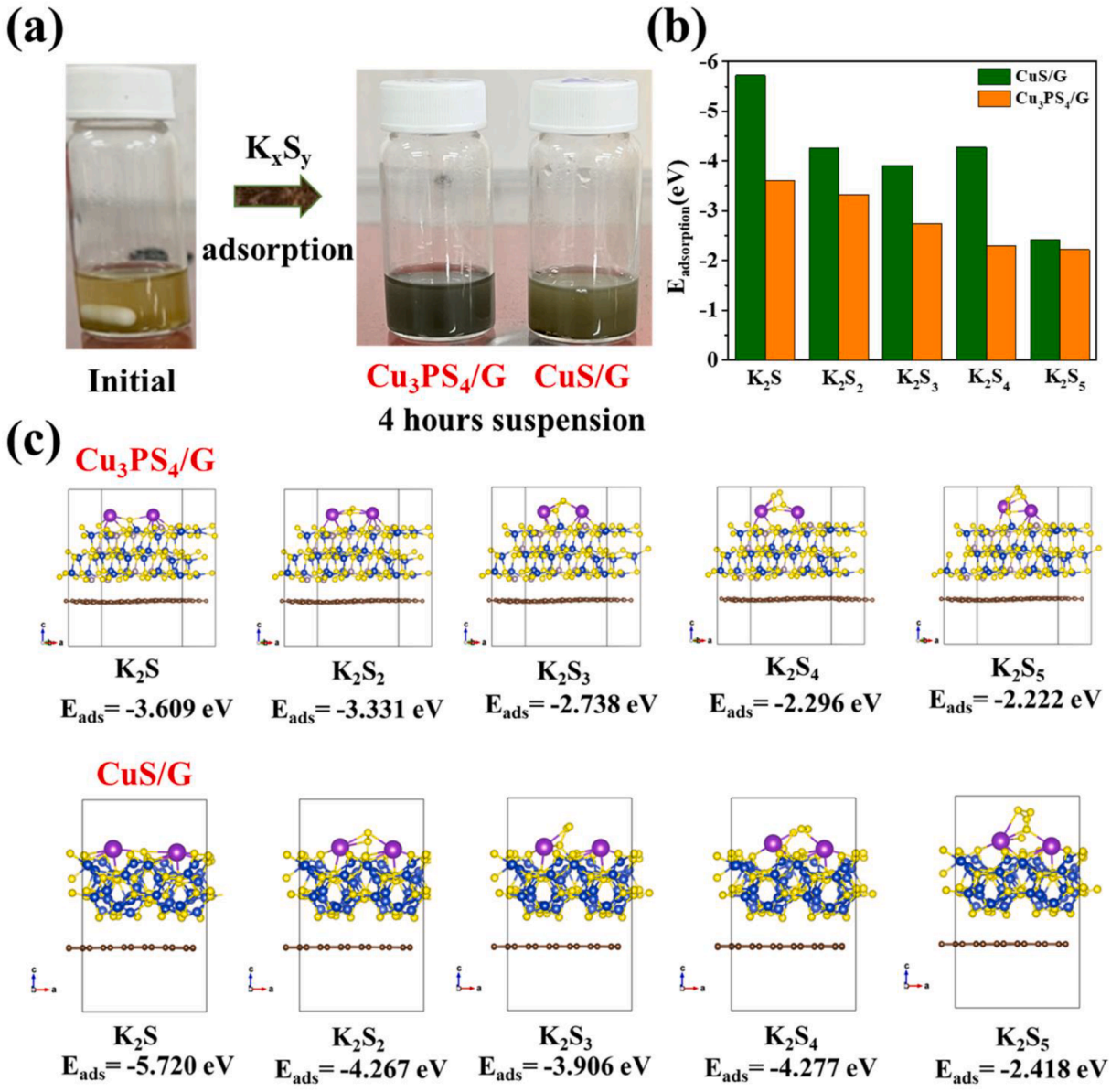

Fig. 6. Potassium polysulfides adsorption experiment. (a) Chemical adsorption method performed by CuS/G and Cu_3PS_4/G for four-hour suspension. (b) The corresponding adsorption energy of CuS/G and Cu_3PS_4/G plotted corresponded with the DFT calculation result. (c) Crystal model of the potassium polysulfides adsorption of CuS/G and Cu_3PS_4/G with their adsorption energy.

optimal tunnel for ion and electron passage, large potassium ions can mobile rapidly in the structure to improve sluggish kinetics that often occurs in metal sulfides and accumulates electrons on the surface of the structure, resulting in a more excellent surface charge effect. Cu_3PS_4 not only provides a larger ionic contact area than binary CuS, but also increases the redox active sites in electrochemical reactions. The low resistance and diffusion energy barrier make the electrode perform better in long-term cycle test, rate performance, and even promotes energy density in potassium ion battery full-cell and potassium ion hybrid capacitor applications. This reveals Cu_3PS_4 a superior electronic channel that optimizes the electrochemical performance of materials, utilizes a fast ion-exchange mechanism to boost the performance of metal sulfides in PIB systems, and provides new insights into all materials whose pseudocapacitive behavior is diffusion-controlled.

2.7. Potassium-ion full battery and hybrid capacitor

Based on the excellent electrochemical performance of Cu_3PS_4/G in half cells and its superior diffusivity ameliorating the redox shuttle effect which often occurs in chalcogenide electrodes, we combined it with the common cathode materials in potassium ion energy storage systems to assemble PIBs full coin cell. Due to the high oxidation potential of the conversion product K_2S, some cathode materials such as PTCDA [70], $KVPO_4F$ [71] cannot meet the working voltage exceeding 3.5 V; as a result, Prussian analogs with high working voltage and stable capacitance such as KFeHCF [72,73], KMnHCF [74] and KNiHCF [75] are used a lot in recent studies. The schematic diagram of the reaction of the potassium ion full battery system is shown (Fig. 7a), in which the Prussian blue synthesized through the precipitation method which has a stable spinel structure, and can stably receive potassium ions diffused from the negative electrode. The SEM images and XRD pattern are shown (Fig. S12 – Fig. S13), respectively, which proves that Prussian blue corresponded to the database can be confirmed. The CV curves of the Cu_3PS_4/G//KFeHCF full cell are plotted at a scan rate of 0.1 mV s^{-1} (Fig. 7b), and it can be seen that there is an oxidation reaction at the first charge near 3.85 V, which is the solid-electrolyte interface film

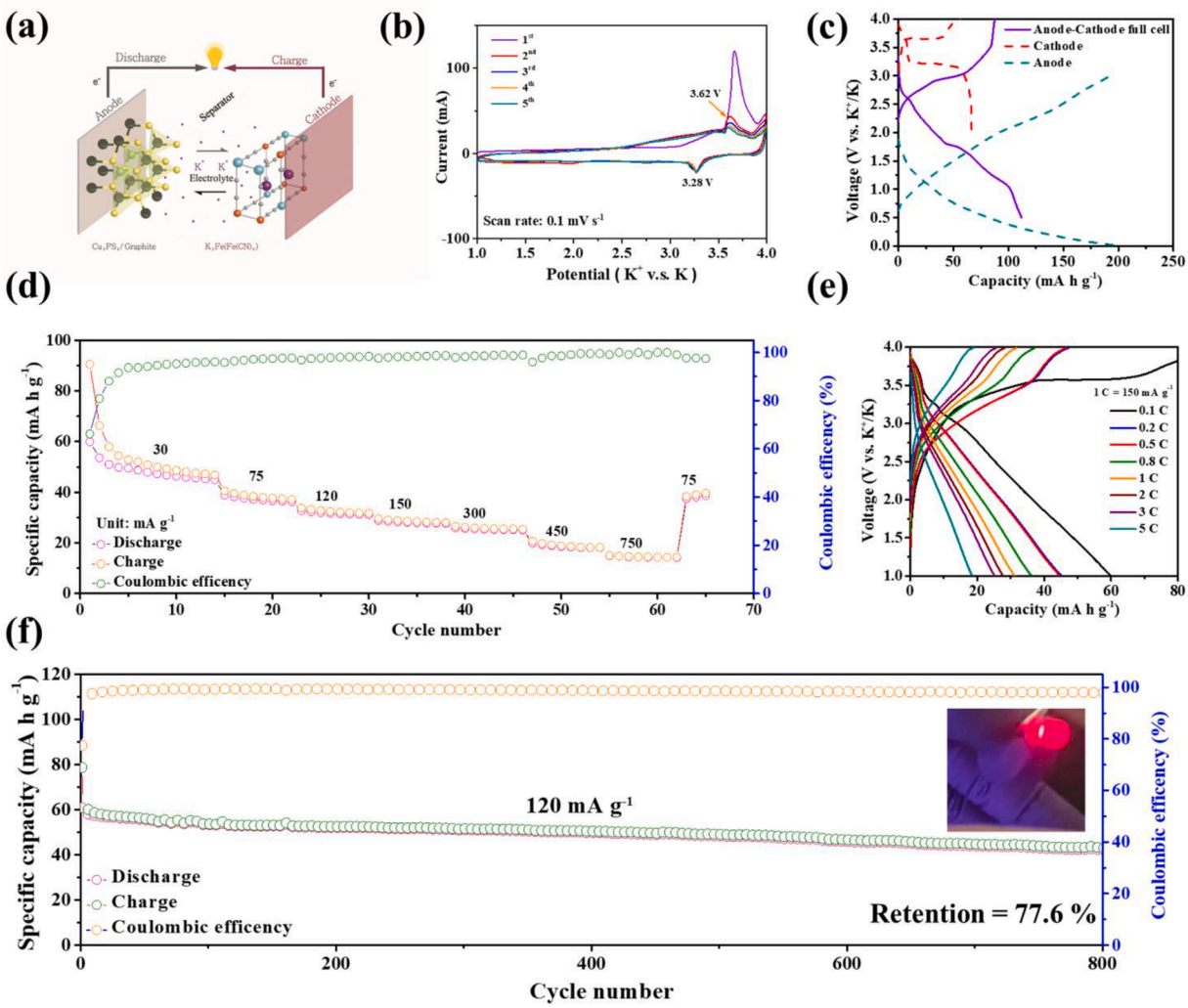

Fig. 7. Potassium ion coin type full cell of Cu_3PS_4/G // PB. (a) Schematic illustration of the full cell operation. (b) CV curves of the full cell at 1st ~ 5th cycle. (c) QV curves of PB cathode, Cu_3PS_4/G anode and full cell. (d) Rate performance at seven different current densities. (e) GCD curves plotted corresponded to rate performance. (f) Long-term cycling performance at 120 mA g^{-1} and LED light demo.

formation. After the second lap, the CV curves are all well-overlapped, showing the high reversibility of the chemical reaction, and the redox reaction of the conversion in the anode provides a lot of specific capacity. In addition, we also measured the rate performance of the Cu_3PS_4/G//KFeHCF full cell (Fig. 7d) at 30, 75, 120, 150, 300, 450, 750 mA g^{-1}, providing capacities of 58, 39, 37, 30, 27, 25, 20 mA h g^{-1}, respectively. The discharge capacity loss in each interval is about 5–10 %. When the current density returned to 75 mA g^{-1}, Cu_3PS_4/G// KFeHCF still had a discharge capacity of 42.5 mA h g^{-1}. Even at high current densities, there would be a slight overpotential shift, resulting in a plateau shift, the Cu_3PS_4/G and Prussian blue still exhibit excellent energy density, while the GCD curves plotted corresponded to the as-tested rate performance at various current densities are shown (Fig. 7e). Finally, our long-term cycle tests based on the total active material weight (Fig. 7f) illustrates that the full cell of PIBs of Cu_3PS_4/G//KFeHCF can maintain a cycle life of 800 cycles at a current density of 120 mA g^{-1} and possess 57 mA h g^{-1} of the reversible capacity. In addition, a fully charged (3.99 V) button-type full battery can be assembled and applied to a LED light demo as shown in the inset of Fig. 7f, which further proves the application potential of the full cell.

Furthermore, we assembled a potassium-ion hybrid capacitor composed of a Cu_3PS_4/G anode and an activated carbon (AC) cathode. With the fast diffusion of potassium ions in the composites and excellent kinetic properties, the FSI-ions in the electrolyte can undergo a Faradaic reaction on the surface of the anode through electrochemical double-layer capacitance (EDLC), and then react on the activated carbon on the surface of the cathode by adsorption and desorption to obtain high energy density. Before assembling the PIHC, we preactivated the Cu_3PS_4/G of the anode for 20 cycles in order to activate the electrode, so that the interior of the material is inserted with potassium ions. Considering the decomposition of the electrolyte at high working voltage, we set the working range at 0.5–3.9 V. The GCD curve is shown (Fig. 8a), and the curve slightly forms a non-isosceles triangle from the ideal triangular shape, which is a reasonable platform displacement and also demonstrates the additional contribution of the pseudo-capacitance to the charge storage. The CV curves of PIHC exhibits a typical capacitive behavior compared with the obvious redox peak in the half-cell due to the complete adsorption–desorption physical reaction (Fig. 8b), which also proves that no other side reactions occur at the working electrode. In addition, CV curves at various scan rates are shown (Fig. 8c) to perform the capacitance contribution. On the other hand, we tested the rate capability of PIHC, based on the total weight of Cu_3PS_4/G and active carbon (Fig. 8d), the energy density of 92, 85, 79, 73, 70, 69, 63 W h kg^{-1} at current densities of 0.1, 0.5, 1, 2, 3, 4, 5, 6 A g^{-1}, respectively. When the current density was restored to 0.1 A g^{-1}, the energy density of PIHC could still reach 89 W h kg^{-1}, showing its extraordinary reversibility. In addition, we compare the energy density and power density of PIHC of chalcogenide anodes in recent years

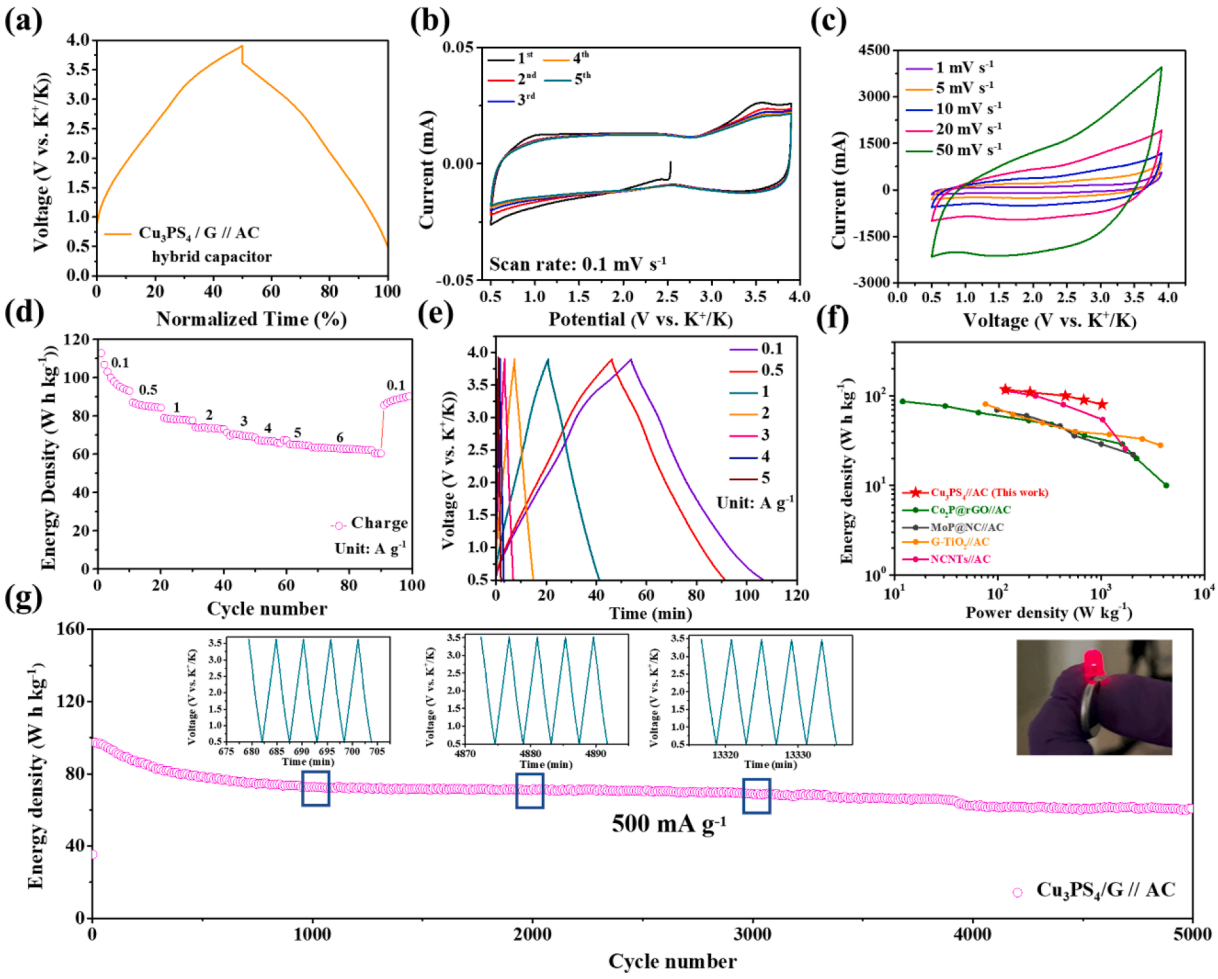

Fig. 8. Potassium ion coin type hybrid capacitor of Cu_3PS_4/G // AC. (a) Normalized GCD curves of the PIHC. (b) CV curves at 0.1 mV s^{-1} at 1st ~ 5th cycle. (c) CV curves of PIHC at various scan rates. (d) Rate performance. (e) Normalized GCD curves plotted corresponded to rate capability. (f) Ragone plot of recent researches of PIHC. (g) Long-term cycling performance at 500 mA g^{-1} and LED light demo. The inset displays the normalized GCD curves at 1000th, 2000th, and 3000th cycle.

through Ragone diagram (Fig. 8f). The long-term cycling performance of PIHC at 500 mA g^{-1} is demonstrated (Fig. 8g), which provides an energy density of 80.3 W h kg^{-1} for over 5000 cycles with 76 % energy density retention, and the battery was applied to LED light demo, showing its potential at energy storage device. Furthermore, we show that the Cu_3PS_4/G//AC performed an energy density of 57 W h kg^{-1} at high current density (Fig. S15), and using 1 M KFSI in DMC as the electrolyte may be more stable for the hybrid capacitor system than choosing 4 M KFSI DME. Based on the outstanding potassium ion diffusivity and sufficient potassium sulfide adsorption energy, the material has excellent performance in hybrid capacitors.

3. Conclusion

This study proposes an electrode with efficient potassium ion diffusion to create a fast ionic channel during charge and discharge, suggesting the synergistic effect of multi-elements in orthorhombic Cu_3PS_4/G to promote the highly-reversible conversion reaction of elements to perform capacities>600 mA h g^{-1}. Compared with some materials whose capacitance contribution is dominated by surface reaction, Cu_3PS_4/G enhances charge transfer through fast ion–electron reaction channels, reduces electrode resistance, and increases the diffusion coefficient of potassium-ions by an order of magnitude, achieving 10^{-9} cm^2 s^{-1}, and exhibits excellent rate performance that can withstand high current densities of 8 A g^{-1}. In addition, the lattice model of potassium ions during diffusion was simulated by the density functional theory, and the difference in the diffusion energy barrier of ternary and binary metal sulfides was compared by the results calculated by the energy barrier, and it was explained that effective adsorption energy of potassium polysulfides, interactively verified the experimental results. During the potassiation–de-potassiation process, it forms a distinct and tight junction to illustrate the structure remains unchanged after charge and discharge, and generates a phase state that provides stable reversible capacitance. Finally, we successfully demonstrated that Cu_3PS_4/G have high energy density and Coulomb efficiency in hybrid capacitors and batteries, giving a proof-of-concept in new energy storage devices. This research not only brings a new perspective in the use of ternary metal sulfides in high-efficiency potassium ion electrode materials, but also solves the shuttle effect and sluggish kinetics that often occur in K-S batteries.

4. Experimental section

4.1. Chemicals and materials

Commercial copper particles (less than425 μm, 99.5 % purity), phosphorus pentasulfides (>99 % purities), Copper sulfate pentahydrate, were purchased from Sigma-Aldrich. Sulfur powder (>99 % purities) was purchased from Alfa-Aesar.

4.2. Preparation of Cu_3PS_4

In a typical synthesis process, 6 mmol of commercial copper particles, 1 mmol of P_2S_5, and 3 mmol of sulfur were ball-milled in a planetary jar containing 4 zirconium balls for 24 h at 400 rpm. For the use of ball mill, the ball to powder weight ratio was set to 5: 1.

4.3. Preparation of Cu_3PS_4/G composites

The Cu_3PS_4/G composites were synthesized by adding 100 mg the as-synthesized Cu_3PS_4 powder and 30 mg graphite in a zirconium jar, and then ball mill for 12 h at 400 rpm.

4.4. Synthesis of CuS nanoparticles

The CuS nanowires were synthesized via a solvothermal method. Typically, 1 mmol copper pentasulfides and 2 mmol of thiourea powder were dissolved in 50 ml DI water. The solution was fully-mixed until it formed a clear solution, and the obtained solution was transferred into a Teflon-lined in an autoclave for 2 h. The black precipitation was centrifugated by absolute ethanol for five times and dried at 80 for further use.

4.5. Synthesis of CuS/G composites

The CuS/G composite were prepared via a ball-milling process. First, 100 mg of the as-synthesized CuS were added with 33 mg of graphite in a zirconia jar. Then 400 rpm ball-milling process was applied for 12 h.

4.6. Synthesis of $K_xFe[Fe(CN)_6]\cdot y\ H_2O$

In a typical synthesis process, 5 mmol of $FeCl_2$ 4 H_2O was dissolved in 100 ml of DI water to be solution A, while 5 mmol of $K_4Fe(CN)_6$3 H_2O, 10 mmol potassium citrate, and excess potassium chloride were dissolved in DI water to form solution B. Then, solution A was slowly added into solution B by precipitation method, and waited for a six-hour suspension. After that, the product was centrifugated and washed for three times with a mixture of DI water, and finally dried at 80 °C in a CVD for 2 h.

4.7. Electrochemical characterization

The Cu_3PS_4/G nano-composite electrodes were fabricated by mixing the active material (Cu_3PS_4/G, 70 wt%), super P (20 wt%), and sodium carboxymethyl cellulose (NaCMC, 10 wt%) in 0.5 ml de-ionized water to form a homogeneous slurry that has 9.5 % solid content. Then, the slurry was casted on the copper foil and dried at 80 °C under argon atmosphere for 90 min to remove residual water and excess solvent. Before coin cell assembly, the electrode is shaped to a circle with 12 mm diameter and densely pressed with a rolling machine. All coin cells were assembled in an argon-filled glove box. We used 1 M KFSI dissolved in 10 ml dimethyl carbonate (DMC) as the electrolyte for potassium-ion half coin cell, Finally, electrochemical performance of Cu_3PS_4/G is tested using Neware series and VMP3 instrument.

4.8. Computational section

The present first principle DFT calculations are performed by Vienna Ab initio Simulation Package (VASP) [1] with the projector augmented wave (PAW) method [2]. The exchange-functional is treated by generalized gradient approximation (GGA) of Perdew-Burke-Ernzerhof (PBE) [3] functional. The energy cutoff for the plane wave basis expansion was set to 450 eV and the force on each atom less than 0.02 eV/Å was set for convergence criterion of geometry relaxation.15 Å vacuum was added along the z direction in order to avoid the interaction between periodic structures. The Brillouin zone integration are sampled by single Γ point for both CuS-graphite and Cu_3PS_4-graphite, respectively. The self-consistent calculations apply a convergence energy threshold of 10^{-5} eV. The DFT-D3 method was employed to consider the van der Waals interaction [4]. Transition state searching were calculated using the climbing-image nudged elastic band (CI-NEB) method [5]. The adsorption energy of K_2S_x molecules were calculated according to.

$$E_{ads} = E_{total} - E_{sub} - E_{mol}$$

where E_{total} is the total energy of the K_2S_x adsorbed systems, E_{sub} and E_{mol} are the energies of the substrate and the isolated K_2S_x molecule, respectively.

4.9. Potassium-ion full cell of Cu_3PS_4 /G // $K_xFe[Fe(CN)_6]\cdot y\ H_2O$

The CR2032 potassium-ion coin type full cell was assembled by setting the cathode-to-anode overall mass ratio to be 5. Before full cell assembly, both anode and cathode were preactivated for 20 cycles and discharge to 0.01 V followed by constant voltage process to maintain the state of the electrodes. Then, 1 M KFSI in DMC was applied as electrolyte and the working window of the full cell was set between 1 V ~ 3.99 V.

4.10. Potassium-ion hybrid capacitor of Cu_3PS_4 /G // AC

The potassium-ion hybrid capacitor was assembled by using Cu_3PS_4/G for anode and active carbon for cathode, with an overall mass ratio to be 1. Before the hybrid capacitor assembly, the anode was preactivated for 10 cycles and discharge to 0.01 V. Afterwards, we used 1 M KFSI in DMC as the electrolyte and set the working window of the hybrid capacitor between 0.5 V ~ 3.99 V.

Declaration of Competing Interest

The authors declare that they have no known competing financial interests or personal relationships that could have appeared to influence the work reported in this paper.

Data availability

No data was used for the research described in the article.

Acknowledgements

This work was supported by the financial support from the 2030 Cross-Generation Young Scholars Program by Ministry of Science and Technology, Taiwan (MOST 111-2628-E-007 -008). H.-Y. Tuan also acknowledges the financial support of National Tsing Hua University, Taiwan, through the grant of 111QI030E1.

Appendix A. Supplementary data

Supplementary data to this article can be found online at https://doi.org/10.1016/j.cej.2022.139199.

References

[1] J. Peng, D. Wu, F. Song, S. Wang, Q. Niu, J. Xu, P. Lu, H. Li, L. Chen, F. Wu, High current density and long cycle life enabled by sulfide solid electrolyte and dendrite-free liquid lithium anode, Adv. Funct. Mater. 32 (2) (2022) 2105776.
[2] H. Liu, M. Li, M. Xiang, J. Guo, H. Bai, W. Bai, X. Liu, Effects of crystal structure and plane orientation on lithium and nickel co-doped spinel lithium manganese oxide for long cycle life lithium-ion batteries, J. Colloid Interface Sci. 585 (2021) 729–739.
[3] W. Yao, S. Wu, L. Zhan, Y. Wang, Two-dimensional porous carbon-coated sandwich-like mesoporous SnO2/graphene/mesoporous SnO2 nanosheets towards high-rate and long cycle life lithium-ion batteries, Chem. Eng. J. 361 (2019) 329–341.
[4] P. Sun, X. Li, J. Shao, P.V. Braun, High-performance packaged 3D lithium-ion microbatteries fabricated using imprint lithography, Adv. Mater. 33 (1) (2021) 2006229.

[5] Q. Li, W. Xue, X. Sun, X. Yu, H. Li, L. Chen, Gaseous electrolyte additive BF3 for high-power Li/CFx primary batteries, Energy Storage Mater. 38 (2021) 482–488.
[6] B. Yang, J. Chen, B. Liu, Y. Ding, Y. Tang, X. Yan, One dimensional graphene nanoscroll-wrapped MnO nanoparticles for high-performance lithium ion hybrid capacitors, J. Mater. Chem. A 9 (10) (2021) 6352–6360.
[7] W. Yan, J. Su, Z.M. Yang, S. Lv, Z. Jin, J.L. Zuo, High-performance lithium-ion capacitors based on porosity-regulated zirconium metal − organic frameworks, Small 17 (22) (2021) 2005209.
[8] X. Liu, J.Q. Huang, Q. Zhang, L. Mai, Nanostructured metal oxides and sulfides for lithium–sulfur batteries, Adv. Mater. 29 (20) (2017) 1601759.
[9] G. Lu, J. Zheng, C. Jin, T. Yan, L. Zhang, J. Nai, Y. Wang, Y. Liu, T. Liu, X. Tao, Lithiated aromatic biopolymer as high-performance organic anodes for lithium-ion storage, Chem. Eng. J. 409 (2021), 127454.
[10] Y. Chen, Z. Yu, P. Rudnicki, H. Gong, Z. Huang, S.C. Kim, J.-C. Lai, X. Kong, J. Qin, Y. Cui, Steric effect tuned ion solvation enabling stable cycling of high-voltage lithium metal battery, J. Am. Chem. Soc. 143 (44) (2021) 18703–18713.
[11] M. Zhang, Y. Li, F. Wu, Y. Bai, C. Wu, Boost sodium-ion batteries to commercialization: Strategies to enhance initial coulombic efficiency of hard carbon anode, Nano Energy 82 (2021), 105738.
[12] X.X. Luo, W.H. Li, H.J. Liang, H.X. Zhang, K.D. Du, X.T. Wang, X.F. Liu, J.P. Zhang, X.L. Wu, Covalent organic framework with highly accessible carbonyls and π-cation effect for advanced potassium-ion batteries, Angew. Chem. Int. Ed. 61 (10) (2022) e202117661.
[13] J. Liao, X. Zhang, Q. Zhang, Q. Hu, Y. Li, Y. Du, J. Xu, L. Gu, X. Zhou, Synthesis of KVPO4F/carbon porous single crystalline nanoplates for high-rate potassium-ion batteries, Nano Lett (2022).
[14] J. Hao, K. Xiong, J. Zhou, A.M. Rao, X. Wang, H. Liu, B. Lu, Yolk–Shell P3-Type K0. 5 [Mn0. 85Ni0. 1Co0. 05] O2: A Low-Cost Cathode for Potassium-Ion Batteries, Energy & Environmental Materials 5(1) (2022) 261-269.
[15] K.S. Lakshmi, X. Ji, L.-D. Shao, B. Vedhanarayanan, T.-W. Lin, Tailor-made organic polymers towards high voltage aqueous ammonium/potassium-ion asymmetric supercapacitors, Appl. Surf. Sci. 577 (2022), 151918.
[16] C. Gao, Y. Lei, Y. Wei, H. Wang, F. Yuan, F. Kang, D. Zhai, Coexistence of two coordinated states contributing to high-voltage and long-life Prussian blue cathode for potassium ion battery, Chem. Eng. J. 431 (2022), 133926.
[17] C.-H. Chang, K.-T. Chen, Y.-Y. Hsieh, C.-B. Chang, H.-Y. Tuan, Crystal facet and architecture engineering of metal oxide nanonetwork anodes for high-performance potassium ion batteries and hybrid capacitors, ACS Nano 16 (1) (2022) 1486–1501.
[18] P.N. Le Pham, V. Gabaudan, A. Boulaoued, G. Åvall, F. Salles, P. Johansson, L. Monconduit, L. Stievano, Potassium-ion batteries using KFSI/DME electrolytes: Implications of cation solvation on the K+-graphite (co-) intercalation mechanism, Energy Storage Mater. 45 (2022) 291–300.
[19] X. Han, T. Chen, P. Zhang, Y. Qi, P. Yang, Y. Zhao, M. Shao, J. Wu, J. Weng, S. Li, Fast Intercalation in Locally Ordered Carbon Nanocrystallites for Superior Potassium Ions Storage, Adv. Funct. Mater. 32 (10) (2022) 2109672.
[20] J. Zhou, Y. Shen, F. Lv, W. Zhang, F. Lin, W. Zhang, K. Wang, H. Luo, Q. Wang, H. Yang, Ultrathin Metallic NbS2 Nanosheets with Unusual Intercalation Mechanism for Ultra-Stable Potassium-Ion Storage, Adv. Funct. Mater. 2204495 (2022).
[21] F. Yuan, H. Sun, D. Zhang, Z. Li, J. Wang, H. Wang, Q. Wang, Y. Wu, B. Wang, Enhanced electron transfer and ion storage in phosphorus/nitrogen co-doped 3D interconnected carbon nanocage toward potassium-ion battery, J. Colloid Interface Sci. 611 (2022) 513–522.
[22] B. Pandit, E.S. Goda, M. Ubaidullah, S.F. Shaikh, U.T. Nakate, A.P. Khedulkar, D. Kumar, R.-A. Doong, Hexagonal δ-MnO2 nanoplates as efficient cathode material for potassium-ion batteries, Ceram, Int, 2022.
[23] M. Xu, D. Zhou, T. Wu, J. Qi, Q. Du, Z. Xiao, Self-regulation of spin polarization density propelling the ion diffusion kinetics for flexible potassium-ion batteries, Adv. Funct. Mater. 2203263 (2022).
[24] Z. Wu, J. Zou, S. Shabanian, K. Golovin, J. Liu, The roles of electrolyte chemistry in hard carbon anode for potassium-ion batteries, Chem. Eng. J. 427 (2022), 130972.
[25] X. Chen, H. Muheiyati, X. Sun, P. Zhou, P. Wang, X. Ding, Y. Qian, L. Xu, Rational design of tungsten Selenide@ N-doped carbon nanotube for high-stable potassium-ion batteries, Small 18 (5) (2022) 2104363.
[26] D.A. Gribble, Z. Li, B. Ozdogru, E. McCulfor, Ö.Ö. Çapraz, V.G. Pol, Mechanistic elucidation of electronically conductive PEDOT: PSS tailored binder for a potassium-ion battery graphite anode: electrochemical, mechanical, and thermal safety aspects, Adv. Energy Mater. 12 (14) (2022) 2103439.
[27] G. Wang, W. Wang, X. He, J. Li, L. Yu, B. Peng, G. Zhang, nnConcunrent manipulation of anion and cation adsorption kinetics in pancake-like carbon achieves ultrastable potassium ion hybrid capacitors, Energy Storage Mater. 46 (2022) 10–19.
[28] F. Yuan, Z. Li, D. Zhang, Q. Wang, H. Wang, H. Sun, Q. Yu, W. Wang, B. Wang, Fundamental understanding and research progress on the interfacial behaviors for potassium-ion battery anode, Adv. Sci. 2200683 (2022).
[29] H. Wu, S. Lu, S. Xu, J. Zhao, Y. Wang, C. Huang, A. Abdelkader, W.A. Wang, K. Xi, Y. Guo, Blowing iron chalcogenides into two-dimensional flaky hybrids with superior cyclability and rate capability for potassium-ion batteries, ACS Nano 15 (2) (2021) 2506–2519.
[30] Q. Pan, Z. Tong, Y. Su, S. Qin, Y. Tang, Energy storage mechanism, challenge and design strategies of metal sulfides for rechargeable sodium/potassium-ion batteries, Adv. Funct. Mater. 31 (37) (2021) 2103912.
[31] L. Cao, B. Luo, B. Xu, J. Zhang, C. Wang, Z. Xiao, S. Li, Y. Li, B. Zhang, G. Zou, Stabilizing intermediate phases via efficient entrapment effects of layered VS4/SnS@ C heterostructure for ultralong lifespan potassium-ion batteries, Adv. Funct. Mater. 31 (36) (2021) 2103802.
[32] C.-B. Chang, K.-T. Chen, H.-Y. Tuan, Large-scale synthesis of few-layered copper antimony sulfide nanosheets as electrode materials for high-rate potassium-ion storage, J. Colloid Interface Sci. 608 (2022) 984–994.
[33] W.-C. Lin, Y.-C. Yang, H.-Y. Tuan, Ternary chalcogenide anodes for high-performance potassium-ion batteries and hybrid capacitors via composition-mediated bond softening and intermediate phase, Energy Storage Mater. (2022).
[34] L. Zhang, M. Zhang, H. Guo, Z. Tian, L. Ge, G. He, J. Huang, J. Wang, T. Liu, I. P. Parkin, A universal polyiodide regulation using quaternization engineering toward high value-added and ultra-stable zinc-iodine batteries, Adv. Sci. 2105598 (2022).
[35] W. Zong, H. Guo, Y. Ouyang, L. Mo, C. Zhou, G. Chao, J. Hofkens, Y. Xu, W. Wang, Y.E. Miao, Topochemistry-driven synthesis of transition-metal selenides with weakened van der waals force to enable 3D-printed Na-ion hybrid capacitors, Adv. Funct. Mater. 32 (13) (2022) 2110016.
[36] Z. Shi, H. Huang, C. Wang, M. Huo, S.-H. Ho, H.-S. Tsai, Heterogeneous transition metal dichalcogenides/graphene composites applied to the metal-ion batteries, Chem. Eng. J. 137469 (2022).
[37] R. Hu, K. Zhu, K. Ye, J. Yan, Q. Wang, D. Cao, G. Wang, Influence of potential range selection on the SnS@ C/rGO anodes in potassium ion battery, Appl. Surf. Sci. 536 (2021), 147832.
[38] Y.-Y. Hsieh, K.-T. Chen, H.-Y. Tuan, A synergetic SnSb-amorphous carbon composites prepared from polyesterification process as an ultrastable potassium-ion battery anode, Chem. Eng. J. 420 (2021), 130451.
[39] J. Deng, X. Huang, M. Wang, M. Xu, Facile synthesis of Cu2S nanoplates as anode for potassium ion batteries, Mater. Lett. 262 (2020), 127048.
[40] J. Li, B. Rui, W. Wei, P. Nie, L. Chang, Z. Le, M. Liu, H. Wang, L. Wang, X. Zhang, Nanosheets assembled layered MoS2/MXene as high performance anode materials for potassium ion batteries, J. Power Sources 449 (2020), 227481.
[41] L. Wang, J. Zou, S. Chen, G. Zhou, J. Bai, P. Gao, Y. Wang, X. Yu, J. Li, Y.-S. Hu, TiS2 as a high performance potassium ion battery cathode in ether-based electrolyte, Energy Storage Mater. 12 (2018) 216–222.
[42] L. Ma, J. Li, T. Wu, P. Sun, S. Tan, H. Wang, W. Xie, L. Pan, Y. Yamauchi, W. Mai, Re-oxidation reconstruction process of solid electrolyte interphase layer derived from highly active anion for potassium-ion batteries, Nano Energy 87 (2021), 106150.
[43] L. Yang, W. Hong, Y. Tian, G. Zou, H. Hou, W. Sun, X. Ji, Heteroatom-doped carbon inlaid with Sb2X3 (X= S, Se) nanodots for high-performance potassium-ion batteries, Chem. Eng. J. 385 (2020), 123838.
[44] K.-T. Chen, S. Chong, L. Yuan, Y.-C. Yang, H.-Y. Tuan, Conversion-alloying dual mechanism anode: Nitrogen-doped carbon-coated Bi2Se3 wrapped with graphene for superior potassium-ion storage, Energy Storage Mater. 39 (2021) 239–249.
[45] W. Wang, J. Zhou, Z. Wang, L. Zhao, P. Li, Y. Yang, C. Yang, H. Huang, S. Guo, Short-range order in mesoporous carbon boosts potassium-ion battery performance, Adv. Energy Mater. 8 (5) (2018) 1701648.
[46] W. Zhang, J. Mao, S. Li, Z. Chen, Z. Guo, Phosphorus-based alloy materials for advanced potassium-ion battery anode, J. Am. Chem. Soc. 139 (9) (2017) 3316–3319.
[47] X. Yu, B. Lu, Z. Xu, Super long-life supercapacitors based on the construction of nanohoneycomb-like strongly coupled CoMoO4–3D graphene hybrid electrodes, Adv. Mater. 26 (7) (2014) 1044–1051.
[48] C. Shen, G. Song, X. Zhu, D. Wang, L. Huang, Z. Sun, Y. Wu, An in-depth study of heteroatom boosted anode for potassium-ion batteries, Nano Energy 78 (2020), 105294.
[49] Z.W. Zhang, H.J. Peng, M. Zhao, J.Q. Huang, Heterogeneous/homogeneous mediators for high-energy-density lithium–sulfur batteries: progress and prospects, Adv. Funct. Mater. 28 (38) (2018) 1707536.
[50] H. Shao, W. Wang, H. Zhang, A. Wang, X. Chen, Y. Huang, Nano-TiO2 decorated carbon coating on the separator to physically and chemically suppress the shuttle effect for lithium-sulfur battery, J. Power Sources 378 (2018) 537–545.
[51] H. Liu, M. Wang, D.D. Zhai, X.Y. Chen, Z.J. Zhang, Design and theoretical study of carbon-based supercapacitors especially exhibiting superior rate capability by the synergistic effect of nitrogen and phosphor dopants, Carbon 155 (2019) 223–232.
[52] J. Tang, C.-Y. Wang, F. Xiu, A.J. Hong, S. Chen, M. Wang, C. Zeng, H.-J. Yang, H.-Y. Tuan, C.-J. Tsai, Single-crystalline Ni2Ge/Ge/Ni2Ge nanowire heterostructure transistors, Nanotechnology 21 (50) (2010), 505704.
[53] J. Li, W. Liu, Z. Yu, J. Deng, S. Zhong, Q. Xiao, D. Yan, N-doped C@ ZnSe as a low cost positive electrode for aluminum-ion batteries: Better electrochemical performance with high voltage platform of~ 1.8 V and new reaction mechanism, Electrochim. Acta 370 (2021), 137790.
[54] X. Yang, Y. Luo, J. Li, H. Wang, Y. Song, J. Li, Z. Guo, Tuning Mixed Electronic/Ionic Conductivity of 2D CdPS3 Nanosheets as an Anode Material by Synergistic Intercalation and Vacancy Engineering, Adv. Funct. Mater. 32 (18) (2022) 2112169.
[55] H.-H. Kim, K.-H. Kim, J. Lee, S.-H. Hong, Electrochemical properties and reaction mechanism of NiTi2S4 ternary metal sulfide as an anode for lithium ion battery, ACS Sustainable Chem. Eng. 9 (29) (2021) 9680–9688.
[56] H. Guo, J. Hu, H. Yuan, N. Wu, Y. Li, G. Liu, N. Qin, K. Liao, Z. Li, W. Luo, Ternary Transition Metal Sulfide as High Real Energy Cathode for Lithium-Sulfur Pouch Cell Under Lean Electrolyte Conditions, Small Methods 6 (2) (2022) 2101402.
[57] W. Yan, K. Liang, Z. Chi, T. Liu, M. Cao, S. Fan, T. Xu, T. Liu, J. Su, Litchi-like structured MnCo2S4@ C as a high capacity and long-cycling time anode for lithium-ion batteries, Electrochim. Acta 376 (2021), 138035.

[58] Y. Wu, S. Hu, R. Xu, J. Wang, Z. Peng, Q. Zhang, Y. Yu, Boosting potassium-ion battery performance by encapsulating red phosphorus in free-standing nitrogen-doped porous hollow carbon nanofibers, Nano Lett. 19 (2) (2019) 1351–1358.
[59] X. Wu, W. Zhao, H. Wang, X. Qi, Z. Xing, Q. Zhuang, Z. Ju, Enhanced capacity of chemically bonded phosphorus/carbon composite as an anode material for potassium-ion batteries, J. Power Sources 378 (2018) 460–467.
[60] H. Wu, G. Chan, J.W. Choi, I. Ryu, Y. Yao, M.T. McDowell, S.W. Lee, A. Jackson, Y. Yang, L. Hu, Stable cycling of double-walled silicon nanotube battery anodes through solid–electrolyte interphase control, Nat. Nanotechnol. 7 (5) (2012) 310–315.
[61] Q. Li, X. Ye, S. Cheng, H. Yu, W. Liu, C.-F. Du, X. Rui, A copper tetrathiovanadate anode for ultra-stable potassium-ion storage, Mater. Chem. Front. 6 (1) (2022) 63–70.
[62] G. Suo, S.M. Ahmed, Y. Cheng, J. Zhang, Z. Li, X. Hou, Y. Yang, X. Ye, L. Feng, L. Zhang, Heterostructured CoS2/CuCo2S4@ N-doped carbon hollow sphere for potassium-ion batteries, J. Colloid Interface Sci. 608 (2022) 275–283.
[63] Y. Cao, Y. Zhang, H. Chen, S. Qin, L. Zhang, S. Guo, H. Yang, Cu12Sb4S13 Quantum Dots/Few-Layered Ti3C2 Nanosheets with Enhanced K+ Diffusion Dynamics for Efficient Potassium Ion Storage, Adv. Funct. Mater. 32 (6) (2022) 2108574.
[64] S. Haghighat-Shishavan, M. Nazarian-Samani, M. Nazarian-Samani, K.-B. Kim, Electrolyte modulation of BiPS4 concurrently suppressing the Bi coarsening and polysulfide shuttle effect in K-ion batteries, Energy Storage Mater. 39 (2021) 96–107.
[65] G.D. Park, J.-S. Park, J.K. Kim, Y.C. Kang, Metal sulfoselenide solid solution embedded in porous hollow carbon nanospheres as effective anode material for potassium-ion batteries with long cycle life and enhanced rate performance, Chem. Eng. J. 428 (2022), 131051.
[66] W. Zhang, J. Chen, Y. Liu, S. Liu, X. Li, K. Yang, L. Li, Decoration of hollow nitrogen-doped carbon nanofibers with tapered rod-shaped NiCo2S4 as a 3D structural high-rate and long-lifespan self-supported anode material for potassium-ion batteries, J. Alloys Compd. 823 (2020), 153631.
[67] X. Chen, N. Cheng, L. Zhang, G. Xiang, Y.-L. Ding, Z. Liu, Flower-like spherical FeCoS2 coated by reduced graphene oxide as anode for high performance potassium ion storage, J. Alloys Compd. 861 (2021), 158458.
[68] X. Ren, D. Yu, L. Yuan, Y. Bai, K. Huang, J. Liu, S. Feng, In situ exsolution of Ag from AgBiS 2 nanocrystal anode boosting high-performance potassium-ion batteries, J. Mater. Chem. A 8 (30) (2020) 15058–15065.
[69] S.-C. Lu, M.-C. Hsiao, M. Yorulmaz, L.-Y. Wang, P.-Y. Yang, S. Link, W.-S. Chang, H.-Y. Tuan, Single-crystalline copper nano-octahedra, Chem. Mater. 27 (24) (2015) 8185–8188.
[70] J. Wang, Z. Xu, J.-C. Eloi, M.-M. Titirici, S.J. Eichhorn, Ice-templated, sustainable carbon aerogels with hierarchically tailored channels for sodium-and potassium-ion batteries, Adv. Funct. Mater. 32 (16) (2022) 2110862.
[71] X.-D. He, L.-M. Zhang, C.-H. Jiang, C.-H. Chen, Elevating cyclability of an advanced KVPO4F cathode via multi-component coating strategy for high-performance potassium-ion batteries, Chem. Eng. J. 433 (2022), 134634.
[72] A. Zhou, W. Cheng, W. Wang, Q. Zhao, J. Xie, W. Zhang, H. Gao, L. Xue, J. Li, Hexacyanoferrate-type Prussian blue analogs: principles and advances toward high-performance sodium and potassium ion batteries, Adv. Energy Mater. 11 (2) (2021) 2000943.
[73] Z. Wang, W. Zhuo, J. Li, L. Ma, S. Tan, G. Zhang, H. Yin, W. Qin, H. Wang, L. Pan, Regulation of ferric iron vacancy for Prussian blue analogue cathode to realize high-performance potassium ion storage, Nano Energy 98 (2022), 107243.
[74] T. Hosaka, T. Fukabori, H. Kojima, K. Kubota, S. Komaba, Effect of particle size and anion vacancy on electrochemical potassium ion insertion into potassium manganese hexacyanoferrates, ChemSusChem 14 (4) (2021) 1166–1175.
[75] L. Li, Z. Hu, Y. Lu, C. Wang, Q. Zhang, S. Zhao, J. Peng, K. Zhang, S.L. Chou, J. Chen, A low-strain potassium-rich Prussian blue analogue cathode for high power potassium-ion batteries, Angew. Chem. 133 (23) (2021) 13160–13166.